# The Evolutions and Large-scale Mechanisms of Summer Stratospheric Ozone Intrusion across Global Hotspots

Jae Won Lee[1], Yutian Wu[1], and Xinyue Wang[2]

[1]Lamont-Doherty Earth Observatory of Columbia University
[2]University of colorado boulder

September 11, 2023

## Abstract

Stratospheric ozone intrusions have a significant impact on surface ozone levels. Especially in summer, intrusions can contribute to extreme ozone events because of preexisting high ozone levels near the surface and cause serious health issues. Considering the increasing trend of surface ozone level, an understanding of stratospheric ozone intrusion is necessary. Previous studies mainly focused on the case studies, and general knowledge of the spatial structure and large-scale dynamics underlying these intrusions is lacking. Thus, based on the Whole Atmosphere Community Climate Model, version 6 (WACCM6) simulation and a stratospheric origin ozone tracer, we identify the global hotspots of stratospheric intrusions: North America, Africa, the Mediterranean, and the Middle East, and investigate the underlying large-scale mechanisms. From the trajectory analysis, we find that the upper-level jet drives isentropic mixing near the jet axis and initiates stratospheric ozone intrusion. Subsequently, climatological descent at the lower troposphere brings the ozone down to the surface, which explains the spatial preference of summertime stratospheric intrusion events. Apart from others, the Middle East shows a relatively fast descent, likely related to the Asian summer monsoon circulation.

## Hosted file

972206_0_art_file_11317671_rzccbc.docx available at https://authorea.com/users/656158/articles/661649-the-evolutions-and-large-scale-mechanisms-of-summer-stratospheric-ozone-intrusion-across-global-hotspots

# The Evolutions and Large-scale Mechanisms of Summer Stratospheric Ozone Intrusion across Global Hotspots

**J. Lee[1], Y. Wu[1], and X. Wang[2]**

[1]Lamont-Doherty Earth Observatory of Columbia University, New York, NY

[2]National Center for Atmospheric Research, Boulder, CO

Corresponding author: Jaewon Lee (jaewonl@ldeo.columbia.edu)

**Key Points:**

- There are 4 hotspots of summer ozone extremes due to stratospheric ozone, North America, Africa, the Mediterranean, and the Middle East.
- Summer stratospheric intrusions initiate in the jet axis region near tropopause by isentropic mixing.
- Climatological descent drives vertical transport in the lower troposphere and determines the location of the hotspots.

## Abstract

Stratospheric ozone intrusions have a significant impact on surface ozone levels. Especially in summer, intrusions can contribute to extreme ozone events because of preexisting high ozone levels near the surface and cause serious health issues. Considering the increasing trend of surface ozone level, an understanding of stratospheric ozone intrusion is necessary. Previous studies mainly focused on the case studies, and general knowledge of the spatial structure and large-scale dynamics underlying these intrusions is lacking. Thus, based on the Whole Atmosphere Community Climate Model, version 6 (WACCM6) simulation and a stratospheric origin ozone tracer, we identify the global hotspots of stratospheric intrusions: North America, Africa, the Mediterranean, and the Middle East, and investigate the underlying large-scale mechanisms. From the trajectory analysis, we find that the upper-level jet drives isentropic mixing near the jet axis and initiates stratospheric ozone intrusion. Subsequently, climatological descent at the lower troposphere brings the ozone down to the surface, which explains the spatial preference of summertime stratospheric intrusion events. Apart from others, the Middle East shows a relatively fast descent, likely related to the Asian summer monsoon circulation.



## Plain Language Summary

High ozone concentration near the surface is harmful to human health. Occasionally, a significant amount of ozone in the stratosphere intrudes deep into the troposphere and increases the surface ozone levels. During summer, because background ozone concentration is high, it is easy for the ozone level to surpass the health threshold with additional contribution from stratospheric ozone intrusion. In this study, we advanced our understanding of the summer stratospheric intrusions, where they happen frequently, and what drives them. We identified four

global hotspots of stratospheric ozone intrusion: North America, Africa, the Mediterranean, and the Middle East, which cover areas not well known to be significantly affected in previous studies. We found that upper tropospheric jet dynamics and lower tropospheric descents both play a role in the stratospheric ozone intrusions and determine the locations affected. Based on the mechanisms, we expect to improve our ability to predict when and where summer stratospheric intrusions may occur. Thereby, our findings can also contribute to the establishment of an early warning system for extreme ozone events in summer.

## 1 Introduction

Ozone is one of the most important chemicals in the atmosphere. The ozone layer in the stratosphere absorbs most of the harmful UV radiation and protects the biosphere at the surface. The energy absorbed by ozone is crucial to the thermal balance in the stratosphere and thereby modifies the stratospheric circulation (e.g., Schoeberl & Hartmann, 1991). On the other hand, ozone in the troposphere is detrimental to the biosphere, particularly to plants (e.g., Heck et al., 1982; Pye, 1988; Reich, 1987; Smith et al., 2003). Exposure to high ozone concentrations is harmful to humans also. The World Health Organization (WHO) recommends limiting outdoor activity when 8-hour mean daily maximum ozone levels exceed 50 ppbv (WHO, 2021). Tropospheric ozone is primarily generated by reactions between ozone precursors such as nitrogen oxides (NOx) and Volatile Organic Compounds (VOCs), which originate from both anthropogenic and natural sources (e.g., Finlayson-Pitts & Pitts Jr, 1993). In addition, occasional intrusion of stratospheric ozone into the troposphere can be a major natural source of ozone in certain locations (e.g., Appenzeller & Davies, 1992; Galani et al., 2003; Langford et al., 2015; Lefohn et al., 2011; Lin et al., 2012; Ott et al., 2016; Stohl et al., 2000; Trickl et al., 2014; Wakamatsu et al., 1989; Zanis et al., 2003).

The stratospheric intrusion can happen within multiple phenomena on different temporal and spatial scales, including Rossby wave breaking (Holton et al., 1995), tropopause folding (Shapiro, 1980), cut-off low (Price & Vaughan, 1993), and mesoscale convective system (Poulida et al., 1996). The first three types of events can displace the tropopause on the isentropic surface latitudinally and allow a massive amount of stratosphere-troposphere exchange. Then sequentially, the large-scale disturbances and smaller-scale turbulences irreversibly mix the stratospheric air with the troposphere (Holton et al., 1995; Johnson & Viezee, 1981; Mahlman, 1997). The stratospheric intrusion within the mesoscale convective system is suggested to be initiated from subsidence around the anvil cloud due to mass conservation compensating upwelling tropospheric air. Then, the strong vertical shear can induce differential advection that can wrap the subsidized stratospheric air (Pan et al., 2014; Phoenix et al., 2020). Given the relatively high ozone level in the stratosphere and the fast increment of ozone concentration during the intrusion, it is important to understand the nature of stratospheric ozone intrusion to establish an effective policy and ozone warning system for the local community.

Here, we focus on the stratospheric ozone intrusions that intrude deep into the troposphere, transporting substantial amounts of ozone to near-surface levels and have substantial potential impact on surface air quality. Škerlak et al. (2015) showed that shallow and medium tropopause folds tend to occur near strong climatological wind in the subtropics, while deep folds follow midlatitude storm tracks. A similar difference is also seen in the stratosphere-to-troposphere transport (STT) patterns between normal STTs and deep STTs (Škerlak et al., 2014). Also, Lin et al. (2015) showed more frequent springtime deep intrusions following La Niña winters, although upper tropospheric ozone peaks after El Niño, underscoring different responses by intrusion depth to climate variabilities. Despite their unique and direct impact on the surface compared to general stratospheric intrusion, deep stratospheric intrusion processes have not yet been studied extensively (Stohl et al., 2003).

Moreover, most studies focused on winter or spring intrusions when the intrusion is more frequent and stratospheric ozone is abundant (Breeden et al., 2021; Johnson & Viezee, 1981; Langford et al., 2009; Lin et al., 2012, 2015; Zhao et al., 2021). However, the consequence of summertime intrusions on surface ozone could be more impactful. During summer, photochemical ozone production reaches its peak, and events like thunderstorms, heat waves, and wildfires are more frequent, which could produce ozone precursors (NOx and VOCs) and increase the reaction rate due to high temperature (Gaudel et al., 2018; Jaffe & Wigder, 2012; Lu et al., 2016; Murray, 2016; Solberg et al., 2008). Because the background ozone concentrations are high, surpassing the health threshold with an additional stratospheric contribution is easy. The model results also show that summer stratospheric origin ozone is not negligible and can potentially trigger extreme ozone events near the surface (Wang et al., 2020). In addition, summer stratospheric intrusions likely favor certain geographical locations (Škerlak et al., 2015). Previous studies have shown that the west coast of the United States (Danielsen, 1980; Lefohn et al., 2011, 2012; Wang et al., 2020) and the eastern Mediterranean (Akritidis et al., 2016; Zanis et al., 2014) are influenced by stratospheric intrusion in summer. However, we lack the general statistics that cover the entire globe and mechanisms that unify the events in different locations. As we face an increasing trend of surface ozone (Gaudel et al., 2018), an overall understanding of summer stratospheric intrusion is needed.

The difficulty of intrusion studies is distinguishing the stratospheric contribution in the air, especially once it is mixed with the surroundings. There are some observations from field works and ground observatories, but their spatial coverage or time period is insufficient for a general understanding (Galani et al., 2003; Gronoff et al., 2021; Ott et al., 2016; Trickl et al., 2014; Wakamatsu et al., 1989; Xiong et al., 2022). To overcome these hardships and cover diverse mechanisms, there are multiple approaches like tropopause folding identification algorithms and back trajectory models on reanalysis and model data (e.g., Li et al., 2015; Škerlak et al., 2015). Here, we will use an artificial tracer called stratospheric origin ozone ($O_3S$). $O_3S$ is identical to the ozone in the stratosphere. However, once $O_3S$ passes the tropopause and enters the troposphere, $O_3S$ does not have production routes and is removed at the same rate as ozone. Therefore, tracking the stratospheric contribution throughout time and space is very useful through $O_3S$ (Lin et al., 2012). It also allows us to cover intrusion events regardless of their triggering mechanisms.

In this study, we aim to address three questions about summer stratospheric ozone intrusion using a state-of-the-art chemistry-climate model and a stratospheric origin tracer: 1) Where and how often do we see extreme summer stratospheric ozone intrusion events? 2) What is the pathway for the intrusion? 3) What is the mechanism in common that drives these events across the global hotspots?

## 2 Methods

### 2.1 WACCM6 & $O_3S$

Our study is based on the daily summertime (June-August, JJA) ozone ($O_3$) and $O_3S$ from the WACCM6 experiment. WACCM6 is a high-top chemistry-climate model of the Community Earth System Model version 2 (CESM2). The model has a horizontal resolution of 0.95°x1.25° (latitude x longitude) and 70 hybrid sigma levels in the vertical (~1.1 km resolution near UTLS).

It has high reproducibility on variabilities like sudden stratospheric warmings (SSWs) and physical variables, such as temperature, wind, and chemicals, in the middle atmosphere, leading to a better stratosphere-troposphere coupling than low-top models (Gettelman et al., 2019). WACCM6 shares most of the physical parameterizations as the low-top Community Atmosphere Model version 6 (CAM6) with an additional gravity wave scheme. The model chemistry mechanism covers the troposphere up to the lower thermosphere. WACCM6 has interactive Community Land Model version 5 (CLM5) coupled as default, and our simulation is a fully coupled ocean-atmosphere historical run (BWHIST). In addition to its better performance in stratospheric dynamics, $O_3$ in both the stratosphere and troposphere has higher fidelity than previous versions (Emmons et al., 2020; Gettelman et al., 2019). Therefore, WACCM6 is suitable for our study on summer stratospheric ozone intrusion (Wang et al., 2020). More information about the model schemes and performance is available in Gettelman et al. (2019) and Emmons et al. (2020). The available data period is from 1995 to 2014, but due to the spin-up time of $O_3S$, we analyzed it from 1996. The $O_3S$ tracer is implemented in the model, as Tilmes et al. (2016) demonstrated. This idealized tracer is identical to $O_3$ above the tropopause and is removed via the same removal process as $O_3$ in the troposphere. However, unlike $O_3$, it does not have any production once in the troposphere. The tropopause here is defined following Reichler et al. (2003), which applied the lapse-rate tropopause definition, the lowest level where the temperature lapse-rate decreases to 2 K/km or less (WMO, 1957).

### 2.2 Maximum Covariance Analysis (MCA)

We applied MCA on the daily 850 hPa $O_3$ and $O_3S$ anomalies during JJA 1996-2014 for each hotspot, which will be defined later. The MCA is a statistical method to identify and analyze relationships between two multivariate datasets. It uses Singular Value Decomposition

(SVD) to extract spatial patterns and Principal Component (PC) timeseries of two datasets that maximize the covariance (Bretherton et al., 1992). It can identify mechanisms that explain the covarying patterns of the two variables and is suitable for our study to analyze the covariability between near-surface $O_3$ and $O_3S$. The 850 hPa level is selected to identify the near-surface extreme $O_3$ intrusion events. Although the high-altitude regions, such as the Tibetan Plateau, potentially have a larger influence from the stratosphere because of their proximity to the stratosphere (Škerlak et al., 2019), we aim to understand the dynamics and impact over the regions in which the distance from the tropopause is similar. We defined daily anomalies after removing the linear trend and seasonal cycle for $O_3$ and $O_3S$. We used the Fourier transform on the 19-year average of each day of the year and extracted up to the 4th harmonics to form a seasonal cycle. This way, we could remove some noises from a relatively small number of years.

### 2.3 TRAJ3D model

The TRAJ3D model, a three-dimensional Lagrangian trajectory model, operates solely on wind vectors to determine the tracer's location (Bowman, 1993; Bowman & Carrie, 2002). The input daily wind data is obtained from our WACCM6 experiment. The trajectory calculations are performed every hour, and trajectory locations are output daily. The four-dimensional linear interpolation is conducted on the wind vector (Bowman et al., 2013). A large number of tracers are released at 500 hPa, and the backward trajectory is integrated for a period of five days. Given that five days is considerably shorter than the typical lifetime of ozone in the free troposphere (a few weeks), we treat $O_3S$ as a passive tracer with an infinite lifetime. The stratospheric intrusion is known to be dominated by isentropic mixing near the tropopause (Holton et al., 1995), which occurs at a finer spatial and temporal resolution compared to the given daily vertical velocity. As the pure trajectory model does not incorporate parameterization for convection, mixing, and turbulence, vertical displacement should be considered with potential uncertainties (Smith et al., 2021).

## 3 Results

### 3.1 Global Hotspots of Stratospheric Intrusion Events

Hotspots in our study are defined as where extreme $O_3$ events are frequent, and the stratospheric contribution to these events is significant. Figure 1 shows the number of days per summer (JJA for NH, DJF for SH) when the 850 hPa $O_3$ exceeds 56.7 ppbv and the contribution of $O_3S$ to $O_3$ is greater than 30%. The 850 hPa $O_3$ threshold is based on the summer median (56.7 ppbv) of days when the 900-1000 hPa average $O_3$ exceeds the surface health threshold (50 ppbv; WHO). In summer, the boundary layer is elevated, and the mixing processes are vigorous between 900 and 1000 hPa. In addition to the above two criteria, we further narrowed it to the regions where $O_3S$ accounts for over half of the $O_3$ variability within the hotspots. Specifically, we considered regions where the correlation between anomalous $O_3S$ and $O_3$ is significant, with an R-squared larger than 0.5.

Overall, most stratospheric intrusion events occur in the NH midlatitudes, between 20º and 50ºN (Fig. 1). Conversely, the SH exhibits fewer events mainly due to the low $O_3$ concentration near the surface. The result reveals four global hotspots for stratospheric intrusions: the West coast of North America (NA), the Northwest coast of Africa (Af), the Eastern Mediterranean (MD), and the Middle East near Iran and Pakistan (ME). Other regions, such as the northern Tibetan Plateau and eastern North America and Asia, are not the focus of this study due to low correlations between anomalous $O_3$ and $O_3S$. Interestingly, except for the ME hotspot, the remaining hotspots are the Mediterranean climate regime. These hotspots qualitatively align with the NH hotspots for tropopause folding events documented in previous studies (Škerlak et al., 2015; Sprenger et al., 2003). The small discrepancies could arise from the differing altitudes of focus (near-surface vs. near-tropopause). Among the hotspots, the NA region exhibits the highest frequency, with approximately 15 events per summer, and other hotspots also experience a minimum of six events per summer. A sensitivity test on the ratio threshold consistently highlights these four hotspots as significant unless an exceptionally large threshold is applied (not shown). However, such high thresholds are deemed inappropriate for our discussion as they result in significantly reduced event frequencies.

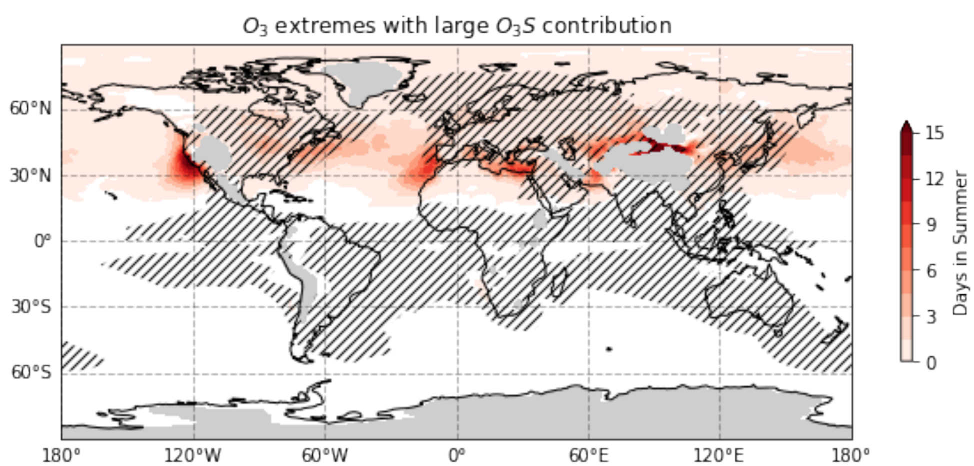


**Figure 1. The average number of summer days during which the 850 hPa $O_3$ exceeds 56.7 ppbv, with 850 hPa $O_3S/O_3$ ratio exceeding 30%. Red shadings are days per summer, and gray shadings are masked topography. Regions where R-squared values between anomalous $O_3$ and $O_3S$ below 0.5 are hatched. The summer period is defined as JJA for NH (19 years) and DJF for SH (18 years starting from Dec 1996).**

We also analyzed the frequencies of events exceeding 99% of all the 850 hPa $O_3S$ across the NH for each season to see where the relative intrusion hotspots are for each season (Fig. S1).

Although summer has the lowest 99% $O_3S$ concentration (19.14 ppbv), it clearly shows the four global hotspots we have seen in Fig. 1. Interestingly, only summer shows such four global hotspots with a strong zonal asymmetry, while other seasons are more zonally symmetric. The NA hotspot always exists throughout the year, but other hotspots disappear in other seasons. Meanwhile, weaker hotspots are seen in different locations in other seasons, for example, over the northern Atlantic and the east coast of North America. This result emphasizes the unique features of summer stratospheric ozone intrusion and its impact on surface ozone extreme events. Also, similar patterns in summer between Fig. 1 and Fig. S1c indicate that stratospheric intrusions are indeed important in extreme ozone events near the surface.

## 3.2 MCA results

We applied the MCA on each identified hotspot between 850 hPa $O_3S$ and $O_3$ to determine the major mechanism for the covariability of the two variables (Fig. S2). In this paper, we will study the leading mode of each hotspot since it is the dominant mode and represents an overall intensification in the region (Fig. 2). The PC timeseries are divided by the standard deviation, and loading vectors are multiplied by that standard deviation. The leading mode outstands the other modes for all the hotspots, especially at the ME hotspot (74.87%). Even the lowest covariance fraction for the leading mode is significantly high (31.96% at the Af hotspot). Thus, the first mode of MCA can represent the large-scale conditions that simultaneously intensify both $O_3S$ and $O_3$.

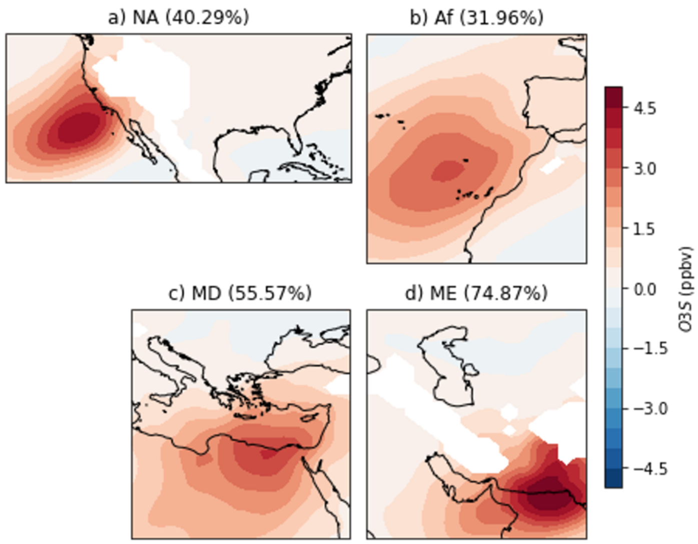


**Figure 2. The 850 hPa $O_3S$ spatial patterns from MCA leading mode are shown for global hotspots: NA, Af, MD, and ME. The MCA has been conducted on the daily 850 hPa $O_3S$ and $O_3$ anomalies in JJA 1996-2014. The covariance fraction explained by the leading mode is written in the parenthesis next to each hotspot.**

The extreme events hereafter are days when both $O_3S$ and $O_3$ PC timeseries for the leading mode exceed one standard deviation level, and we count the continuous extreme days as a single event. We identified 61, 65, 48, and 51 total events in NA, Af, MD, and ME during 19 years, respectively, which is about 3% of the total days in summer (Fig. S3). Although most events last 1-2 days, long-lived events can last as long as 10 days (not shown). Figure 2 shows that NA and Af patterns peak in the nearby ocean, while MD and ME peaks are on the coast with higher population densities, which appear to be more detrimental to nearby communities. Especially the peak concentration in the ME hotspot is the highest among hotspots (Fig. 2). To determine the dominance of the leading mode among all extreme events, we compared the above extreme events associated with the leading mode with events identified in Fig. 1. For each grid over the peaks of hotspot regions, about 30-50% of the MCA-identified events overlap, and the $O_3S$ averages over event days are similar in magnitude (not shown). Therefore, understanding the mechanism of MCA-identified extreme events could help explain many extreme events in the global hotspots.

Extreme events occur irregularly, and the frequency changes over time. There is no clear increasing or decreasing trend in the number of extreme events in any hotspot (not shown). We also analyzed if there is any preference in the timing of events within the summer for each hotspot (Fig. S3). Most locations have a weak intraseasonal variability, except MD, which has a strong intraseasonal variability. The MD hotspot shows a large preference in the early summer and almost no events in August. This is an unexpected result since previous studies emphasized that Etesian wind in the Mediterranean strongly correlates with the intrusion, which peaks in late summer (Dafka et al., 2021; Tyrlis & Lelieveld, 2013). Although a few questions exist in the intraseasonal variability of extreme events, we will focus on the general features of extreme events to understand the commonalities between events.

## 3.3 Trajectory and Upper-level Dynamics

The $O_3S$ anomaly composites were analyzed to examine the typical intrusion patterns utilizing the MCA results. To determine the descending process of the intrusion, the box averaged $O_3S$ anomaly was calculated for every level from 8 days prior to the event up until the event days (Fig. 3). Based on the $O_3S$ composites, a box region was selected to encompass the potential trajectories associated with each hotspot (Fig. S2). The analysis reveals a descent starting from approximately 4-5 days before the events at about 500 hPa. Above 500 hPa, it is challenging to distinguish a descent due to the high background $O_3S$ concentrations.

Consequently, the use of a back trajectory model is necessary to differentiate the intrusion from the background $O_3S$ above 500 hPa.

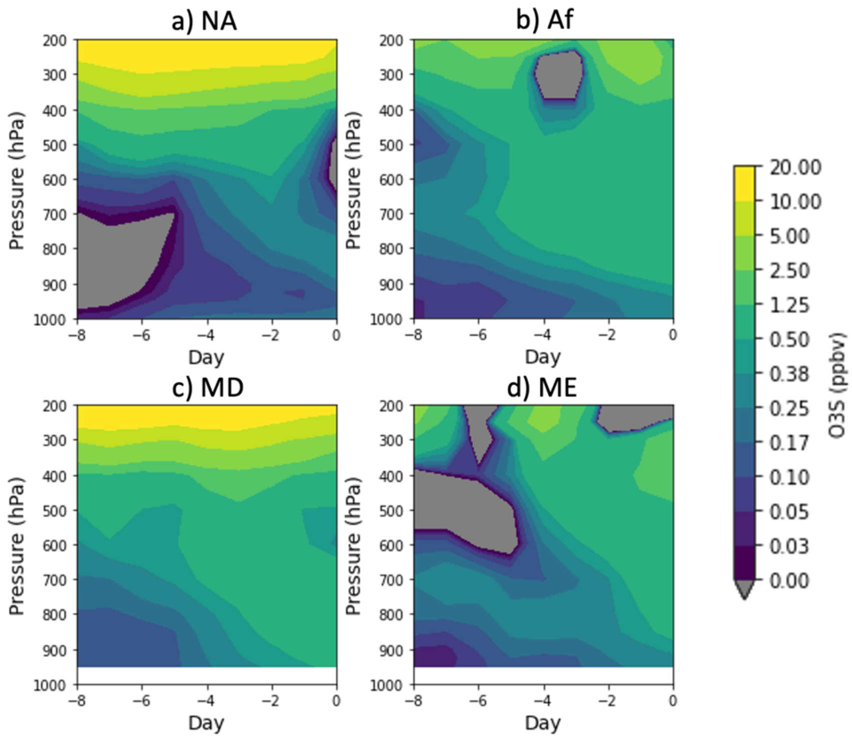


**Figure 3. The box averaged $O_3S$ anomaly for each level from 8 days prior to the events to the event days. The box regions are defined in Fig. S2. The negative values are grayed out. The white areas are topography.**

The TRAJ3D model was employed to estimate the trajectories of summer stratospheric ozone intrusion above 500 hPa. First, a box region enclosing the statistically significant maximum of the 500 hPa $O_3S$ anomaly three days before the events is designated for each hotspot. This specific date is chosen as the intrusion signal at 500 hPa $O_3S$ anomaly displays the most prominence. Subsequently, tracers are released at the significant area of each intrusion case within the assigned box region, where $O_3S$ exceeds one standard deviation in time. Back trajectories are then calculated for a period of 5 days with a large set of tracers. Hereby, 'ensemble' is each extreme stratospheric intrusion case at each hotspot, and 'trajectory' is an individual trajectory among a large set of trajectories for each ensemble, which has different initial locations from each other. Within the significant area for each ensemble, 1000 trajectories are initiated at randomly selected grid points allowing duplication after regridding to 0.5ºx0.5º resolution. For example, the NA hotspot has 61 ensembles, and each ensemble has 1000 trajectories, total of 61000 trajectories (61 ensembles x 1000 trajectories). In different ensembles, both the initial tracer locations and the wind field can change, as significant area and event date differ by the ensemble.

The trajectories for each hotspot are presented in the left column of Fig. 4. The mean trajectories for each ensemble are depicted as gray lines. The colored line shows the mean trajectory for the hotspot, which is the mean of gray lines, with height represented in color. For instance, in the NA hotspot, gray lines show 61 ensembles, which is the mean of 1000 trajectories for each ensemble. The colored line is an average of 61 ensembles, which is the mean of 61000 trajectories. Generally, for all the hotspots, the trajectories exhibit a southeastward descent that crosses the jet axis, which is denoted by the red contours. Consistent with previous studies, the southeastward descending pathway is attributed to the tilted isentropic surfaces and the strong climatological westerlies in the midlatitudes (Akritidis et al., 2016; B. Škerlak et al., 2014; Sprenger & Wernli, 2003). Three hotspots, i.e., NA, Af, and MD, continue their southeastward descent to 850 hPa. However, ME trajectories experience a rapid descent near the 500 hPa into the lower troposphere. Then, the northerly wind transports $O_3S$ toward the 850 hPa hotspot (not shown). We will briefly discuss how the ME hotspot trajectories and governing mechanisms differ from others and how they relate to the Asian summer monsoon in the next section.

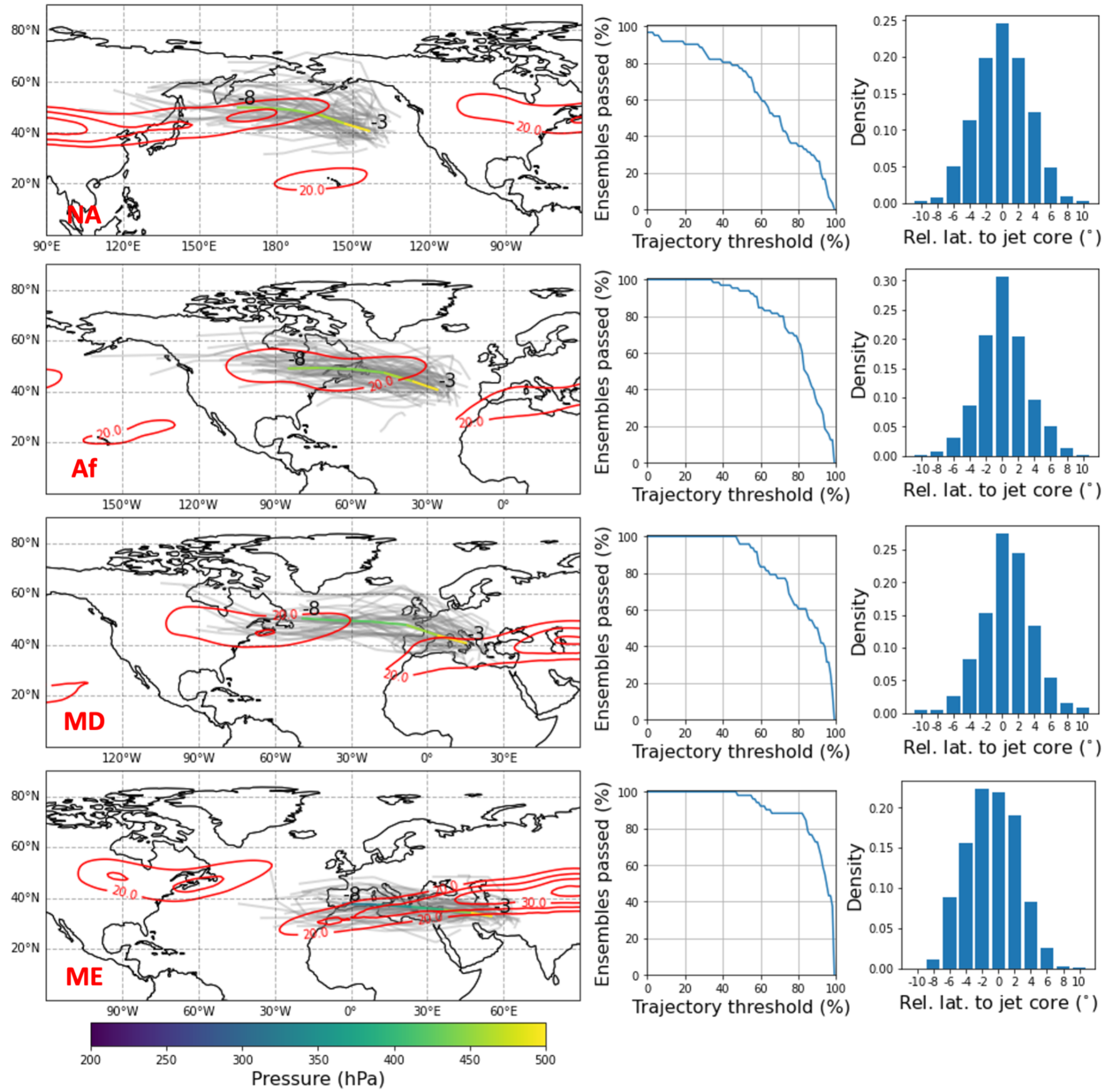


**Figure 4. (left) The back trajectories from the TRAJ3D model within each hotspot. The gray lines indicate ensemble mean trajectories. The colored line shows the mean trajectory across all the ensembles, which is the mean of gray lines, with height represented in color. The red contours are 200 hPa zonal wind averaged over 3 to 8 days before every event. (middle) The percentage of ensembles that pass the jet axis region as a function of trajectory threshold. Any time between 4 days to 8 days before the event, if the trajectory**

**passes the jet between 200 to 300 hPa, the trajectory is considered as crossing the jet axis. Details are explained in the text. (right) The histogram of the relative latitude of trajectories to the jet core at 200 hPa. The day with most tracers passing the jet axis from 4 to 8 days prior to the event is considered. Every bin width is 2°, centered on the values at the x-axis. Each row exhibits results at each hotspot: NA (1st row), Af (2nd row), MD (3rd row), and ME (4th row).**

Previous studies have highlighted that during boreal summer, NH STT exhibits two latitude maxima: one over the midlatitudes and the other over the subtropics (Hsu et al., 2005; Jing et al., 2004; Tang et al., 2011). In the midlatitudes, deep convection over continents plays a significant role, whereas, in the subtropics, it is primarily via Rossby wave breaking (RWB) over the ocean. However, Škerlak et al. (2014) demonstrated that summer deep stratospheric intrusions originate from locations distinct from the mentioned STT maxima. Given the considerable number of ensembles crossing the jet axis, we hypothesize that isentropic mixing near the jet axis is the source of $O_3S$ for deep STT in summer (Holton et al., 1995). We conducted a quantitative analysis to ascertain whether the estimated trajectories intersect the jet axis. Figure 5 presents an example of a single case with the zonal wind at 200 hPa eight days before the event. The tracers are denoted by dots, with tracers in the jet axis region depicted in blue. The jet axis region is defined as where the zonal wind exceeds 20 m/s (red shading). The jet cores are identified as wind maxima latitudes for each longitude. We calculated the number of trajectories that crossed the jet axis region regardless of the level and time. In the case study of Fig. 5, 38.1% of the trajectories are found to cross the jet axis region at the given level and time. The middle column of Fig. 4 summarizes the statistics of all the trajectories and illustrates the trajectory threshold and the corresponding percentage of ensembles that meet the threshold. For instance, a 50% trajectory threshold means that over 50% of the trajectories cross the jet axis. The y-axis represents the percentage of ensembles that pass the test at a given trajectory threshold, normalized by the total number of ensembles within each hotspot. The findings reveal a substantially high percentage of ensembles that pass the test for all hotspots. This indicates that intrusion trajectories have a high possibility of crossing the jet axis region and supports the idea that isentropic mixing near the jet axis is the source of $O_3S$ for deep STT in summer.

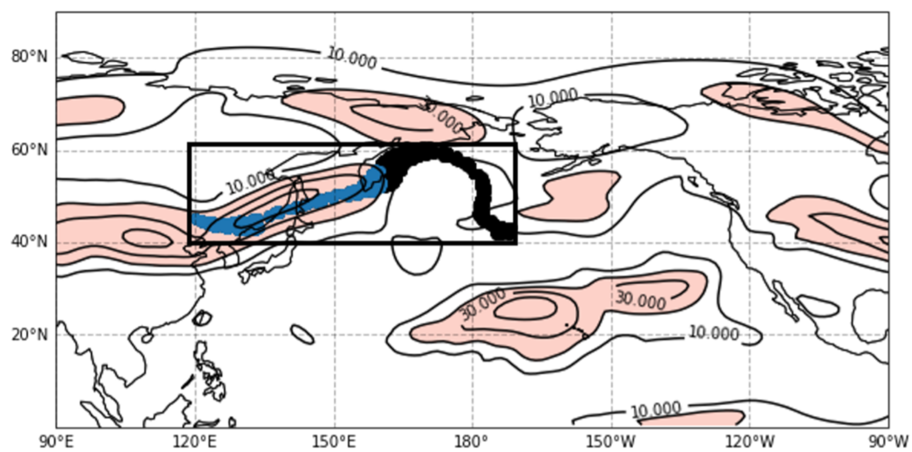


**Figure 5. A case study of tracer ensembles 8 days before the event at 200 hPa. The contours are 200 hPa zonal wind velocity (u). The dots are tracers, and tracers on the jet axis region (red shading; u > 20 m/s) are in blue. The box is assigned to encompass all the tracers.**

We further assessed whether trajectories crossing the jet axis region are statistically significant. For each ensemble, at multiple pressure levels and dates preceding the event (300 hPa, 250hPa, and 200 hPa, 4 to 8 days prior), we computed the area ratio (r) of the jet axis region to the box region enclosing the maximum and minimum latitude and longitude of the tracers (Fig. 5). Assuming a completely random process, each tracer can be considered to follow a binomial distribution with a sample size (N) of 1000. Applying the central limit theorem, this distribution can be approximated by a normal distribution with *Nr* as the mean and *Nr(1-r)* as the variance. Through standardizing, we found that around 80% of the cases exhibit a significance exceeding two standard deviations for each hotspot (2.5%, one-sided). For instance, in the NA hotspot, 79.3% out of 915 cases (61 ensembles x 5 dates x 3 pressure levels) have passed the significance test. The result indicates that, regardless of the time and level, there is a significant likelihood of the trajectory intersecting the jet axis. A sensitivity test was performed by releasing tracers at the maximum within 2 and 4 days before the event, yielding similar substantial probabilities of stratospheric intrusion crossing the jet axis (not shown).

We also examined the potential relationship between the stratospheric intrusion events and RWB, a major driver of isentropic mixing, to determine if any association exists. However, our results did not reveal a significant relationship between the two (not shown). While this finding may differ from previous studies (Holton et al., 1995), we do not consider it contradictory. The events we analyzed may differ from those examined in previous studies, which could lead to variations in the observed relationship.

Furthermore, we investigated the preferred crossing location of trajectories relative to the jet core in terms of latitude at 200 hPa. The location on a day with a maximum number of tracers on the jet axis between 4 to 8 days before the event is examined. As shown in the right column of Fig. 4, the distribution is centered near the core region, with a slight poleward tilt except for the ME hotspot. A sensitivity test on different pressure levels shows a slight shift to the poleward flank on lower pressure levels. Still, it does not affect the general feature of the relative locations (not shown). This finding is consistent with Yang et al. (2016), which noted that summer intrusions exhibit a unique characteristic wherein the peak ozone flux into the troposphere occurs near the core region, while other seasons prefer the poleward flank. The reason for the ME hotspot's preference for the equatorward flank of the jet remains not understood, but it could be attributed to a distinct dynamical mechanism associated with the Asian summer monsoon.

### 3.4 Vertical Transport in the Lower Troposphere

Now that we know the pathway to the mid-troposphere, we further address the question of what contributes to the vertical descent in the lower troposphere. In other words, what is the dynamics that is in common in bringing the $O_3S$ down to the near-surface level? To answer the question, we conducted a budget analysis on the tendency of the $O_3S$ anomaly transport at 850 hPa (600 hPa for ME). The tendency can be decomposed into the following terms:

$$\frac{\partial O3S_a}{\partial t} = -\omega_c \frac{\partial O3S_a}{\partial p} - \omega_a \frac{\partial O3S_c}{\partial p} - \left(\omega_a \frac{\partial O3S_a}{\partial p}\right)_a + (Zonal) + (Meridional) + (Residuals),$$

where subscript *a* indicates anomaly and *c* indicates climatological seasonal cycle. We first decomposed the tendency into zonal, meridional, vertical transport, and residual terms. Then, we further separated vertical transport into contributions from climatological wind ($-\omega_c \frac{\partial O3S_a}{\partial p}$), anomalous wind ($-\omega_a \frac{\partial O3S_c}{\partial p}$), and nonlinear ($-\left(\omega_a \frac{\partial O3S_a}{\partial p}\right)_a$) terms, as the focus is on the mechanism that brings air down. We smoothed the data by taking a 5°x5° moving box mean for each term. Then, we examined the maximum tendency for each pressure level near the hotspots and 10 to 0 days before the events. The analysis reveals a greater magnitude of horizontal transport compared to vertical transport (not shown), which is expected due to larger horizontal wind velocities. However, since our question is on the mechanism of vertical transport to the near-surface level, we focus on the common factors that contribute to the vertical transport across the global hotspots.

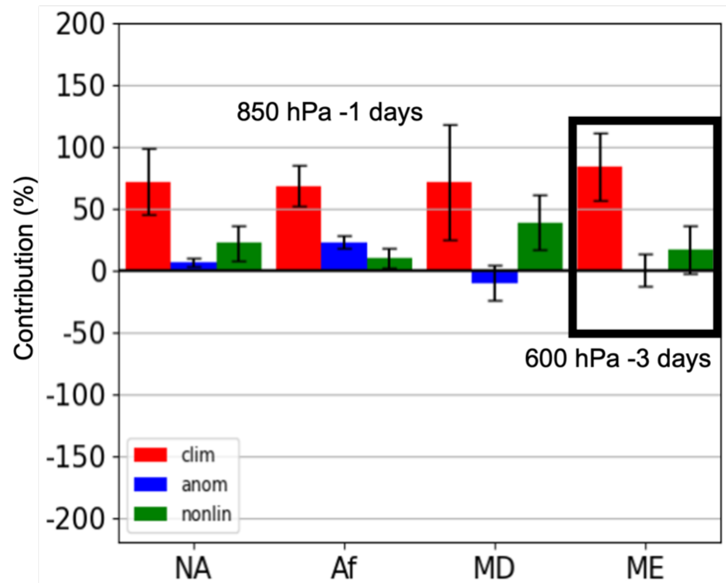


**Figure 6. The relative importance of vertical transport decomposition to the total vertical transport. Red, blue, and green indicate climatological wind-driven, anomalous wind-driven, and nonlinear terms, respectively. The total vertical transport is calculated in the tendency equation on the maximum tendency at a given time and pressure level. To compare with other hotspots, each term in vertical transport is divided by the total vertical transport from the corresponding hotspot. Thus, three terms percentages add up to 100% for each hotspot. Three hotspots (NA, Af, and MD) are calculated on day -1 at 850 hPa, while ME is calculated on day -3 at 600 hPa. The terminations of each term and their formula follow the equation in section 3.4, and a detailed explanation of the time and level selection is given there.**

The role of climatological wind-driven vertical transport is substantial in all hotspots (red bars in Fig. 6). This figure illustrates the vertical transport in the maximum tendency for a day before events at 850 hPa and its decomposition for each hotspot (NA, Af, and MD). Based on the trajectory, the ME hotspot tendency is calculated for -3 days at 600 hPa. We see a gradual descent from the trajectory in three hotspots except ME, where strong descent happens a few days ahead of the event and then horizontally shifts to the event region. The climatological vertical transport dominates in the lower troposphere from 600 to 850 hPa near the hotspots, even out of the maximum tendency region. This climatological dominance explains the co-location of climatological descent regions (mainly the Mediterranean climate regime) and global hotspots of stratospheric intrusion. In addition, it's worth noting that the climatological wind-driven vertical transport also depends on the vertical gradient of the $O_3S$ anomaly. Our understanding is that the upper-level system induces this anomaly, as demonstrated in Section 3.3. Once the gradient is established, the climatological descent transports the anomaly to the near-surface level. The upper-level dynamics that initiate the intrusion is attributable to jet dynamics, as our trajectory results and previous studies suggested (Fig. 3; Wang et al., 2020). Although climatological descent in the lower troposphere does not elucidate all the intrusion processes and determines the location, it has a considerable contribution. This also explains the distinct geographical locations of $O_3S$ extremes in the summer compared to other seasons. The climatological descent is prominent during the summer due to the anticyclone formation in the ocean (NA and Af; Rodwell & Hoskins, 2001) and the Asian summer monsoon (MD and ME; Wu et al., 2018).

The ME hotspot is notable as its strong descending region is far apart from the hotspot region. The $O_3S$ hotspot is located near the coast of Pakistan, while strong descent happens about 10° north. This is an example of horizontal transport moving the descended ozone from one location to another and setting the location of $O_3S$ extremes. Once we focus on the descending period (day -3 at 600 hPa), the climatological descent dominates the vertical transport, as mentioned earlier. The northerly wind that transports $O_3S$ to the hotspot shows a similar pattern to the Asian summer monsoon circulation. In addition, anomalous high precipitation is also observed in the Bay of Bengal two days before the extreme events (not shown). These results are consistent with the large-scale descent and tropopause folds in the Middle East occurring as a result of monsoon dynamics discussed in previous studies (Rodwell & Hoskins, 2001; Wu et al., 2018).

## 4 Conclusion and discussions

We identify summertime stratospheric intrusion hotspots using a state-of-the-art chemistry climate model and a stratospheric origin tracer, and investigate the pathway and mechanism of these intrusion events. Maximum covariance analysis demonstrates that there are four global hotspots with frequent near-surface summer ozone extreme events due to stratospheric intrusion: the West coast of North America (NA), the Northwest coast of Africa (Af), the Eastern Mediterranean (MD), and the Middle East near Iran and Pakistan (ME). To elucidate the trajectory and underlying mechanisms of each hotspot, we employ the Lagrangian pure transport model (TRAJ3D). The stratospheric intrusions above 500 hPa generally follow a southeastward descent and traverse the jet axis as they enter the troposphere. The estimated trajectories align well with previous studies and are potentially driven by isentropic mixing near the tropopause (Škerlak et al., 2014; Yang et al., 2016). Furthermore, budget analysis shows that the climatological descent-driven vertical transport is the governing mechanism for descent from the mid- to the lower- troposphere (below 500 hPa) over all hotspots. This explains the global hotspots being located in the strong climatological descent regions, mostly in the Mediterranean climate regime.

Furthermore, we have shown that deep summer stratospheric intrusion has unique characteristics and affects the regions not much considered earlier, such as the northwest coast of

Africa and near Iran and Pakistan (ME hotspot). Especially the Pakistan region shows extremely high values of stratospheric intrusion. Our analyses suggest the Asian summer monsoon as a possible precursor. Therefore, studies examining the linkage between the Asian summer monsoon and the summer stratospheric intrusion in Pakistan are needed considering their poor background air quality and high population (Anjum et al., 2021; Mehmood et al., 2020).

There are still several unresolved issues regarding summer stratospheric intrusions. The wave dynamics near the upper tropospheric jet and persistent climatological descent cannot explain the rareness of the intrusion events. We propose that these two pieces must be connected with a suitable horizontal wind, which is a potential third key factor, for extreme events to occur. If the ozone flux in the upper troposphere does not reach the climatological descent region, it will not be able to reach the near-surface level. Another possibility is that either the upper-tropospheric wave activities or the climatological descent is extreme during these events. However, the intraseasonal variability of the climatological descent is likely too weak to explain the occurrence of extreme events. A mechanistic study on the upper tropospheric dynamics in summer could fill the gap in our understanding of the summer stratospheric intrusion. The intraseasonal and interannual variability of the summer stratospheric intrusion also needs further study. For example, a strong intraseasonal variability exists in the MD hotspot, with no events in August in this model simulation. Also, the interannual variability of the summer intrusion at the NA hotspot does not show a connection to ENSO (not shown), whereas the spring deep STT increases during La Ninas (Lin et al., 2015; Albers et al., 2022).

Although this study is based on a single chemistry climate model output, it provides a comprehensive analysis of the global hotspots of summertime stratospheric intrusions and their underlying dynamical mechanism. It is worthwhile conducting further studies with a different model and data set to test the robustness. Our findings can potentially contribute to the forecasting of extreme ozone events in summer and benefit policymakers in establishing an early warning system.

**Acknowledgments**

We thank S. Tilmes of the National Center for Atmospheric Research for providing the WACCM6 model results. We also thank K. P. Bowman of Texas A&M University for the TRAJ3D code, W. P. Smith of the National Center for Atmospheric Research for great help with the trajectory analysis, and W. Randel of the National Center for Atmospheric Research for helpful discussion on dynamics. J. L. and Y. W. are supported by the National Science Foundation award AGS-1802248.

**Data Availability Statement**

The processed data used for the analysis in the study are available at Columbia University Academic Commons via (Lee, 2023) All WACCM6 simulations were carried out on the Cheyenne high-performance computing platform and are available at NCAR's Campaign Storage upon acceptance.

**References**

Akritidis, D., Pozzer, A., Zanis, P., Tyrlis, E., Škerlak, B., Sprenger, M., & Lelieveld, J. (2016). On the role of tropopause folds in summertime tropospheric ozone over the eastern Mediterranean and the Middle East. *Atmospheric Chemistry and Physics*, *16*(21), 14025–14039. https://doi.org/10.5194/acp-16-14025-2016

Albers, J. R., Butler, A. H., Langford, A. O., Elsbury, D., & Breeden, M. L. (2022). Dynamics of ENSO-driven stratosphere-to-troposphere transport of ozone over North America. *Atmospheric Chemistry and Physics*, *22*(19), 13035–13048. https://doi.org/10.5194/acp-22-13035-2022

Anjum, M. S., Ali, S. M., Imad-ud-din, M., Subhani, M. A., Anwar, M. N., Nizami, A.-S., et al. (2021). An Emerged Challenge of Air Pollution and Ever-Increasing Particulate Matter in Pakistan; A Critical Review. *Journal of Hazardous Materials*, *402*, 123943. https://doi.org/10.1016/j.jhazmat.2020.123943

Appenzeller, C., & Davies, H. C. (1992). Structure of stratospheric intrusions into the troposphere. *Nature*, *358*(6387), 570–572.

Bowman, K. P. (1993). Large-scale isentropic mixing properties of the Antarctic polar vortex from analyzed winds. *Journal of Geophysical Research: Atmospheres*, *98*(D12), 23013–23027.

Bowman, K. P., & Carrie, G. D. (2002). The mean-meridional transport circulation of the troposphere in an idealized GCM. *Journal of the Atmospheric Sciences*, *59*(9), 1502–1514.

Bowman, K. P., Lin, J. C., Stohl, A., Draxler, R., Konopka, P., Andrews, A., & Brunner, D. (2013). Input data requirements for Lagrangian trajectory models. *Bulletin of the American Meteorological Society*, *94*(7), 1051–1058.

Breeden, M. L., Butler, A. H., Albers, J. R., Sprenger, M., & Langford, A. O. (2021). The spring transition of the North Pacific jet and its relation to deep stratosphere-to-troposphere mass transport over western North America. *Atmospheric Chemistry and Physics*, *21*(4), 2781–2794. https://doi.org/10.5194/acp-21-2781-2021

Bretherton, C. S., Smith, C., & Wallace, J. M. (1992). An Intercomparison of Methods for Finding Coupled Patterns in Climate Data. *Journal of Climate*, *5*(6), 541–560. https://doi.org/10.1175/1520-0442(1992)005<0541:AIOMFF>2.0.CO;2

Dafka, S., Akritidis, D., Zanis, P., Pozzer, A., Xoplaki, E., Luterbacher, J., & Zerefos, C. (2021). On the link between the Etesian winds, tropopause folds and tropospheric ozone over the Eastern Mediterranean during summer. *Atmospheric Research*, *248*, 105161.

Danielsen, E. F. (1980). Stratospheric source for unexpectedly large values of ozone measured over the Pacific Ocean during Gametag, August 1977. *Journal of Geophysical Research: Oceans*, *85*(C1), 401–412.

Emmons, L. K., Schwantes, R. H., Orlando, J. J., Tyndall, G., Kinnison, D., Lamarque, J.-F., et al. (2020). The chemistry mechanism in the community earth system model version 2 (CESM2). *Journal of Advances in Modeling Earth Systems*, *12*(4).

Finlayson-Pitts, B. J., & Pitts Jr, J. N. (1993). Atmospheric chemistry of tropospheric ozone formation: scientific and regulatory implications. *Air & Waste*, *43*(8), 1091–1100.

Galani, E., Balis, D., Zanis, P., Zerefos, C., Papayannis, A., Wernli, H., & Gerasopoulos, E. (2003). Observations of stratosphere-to-troposphere transport events over the eastern Mediterranean using a ground-based lidar system. *Journal of Geophysical Research: Atmospheres*, *108*(D12).

Gaudel, A., Cooper, O. R., Ancellet, G., Barret, B., Boynard, A., Burrows, J. P., et al. (2018). Tropospheric Ozone Assessment Report: Present-day distribution and trends of tropospheric ozone relevant to climate and global atmospheric chemistry model evaluation. *Elementa: Science of the Anthropocene*, *6*.

Gettelman, A., Mills, M. J., Kinnison, D. E., Garcia, R. R., Smith, A. K., Marsh, D. R., et al. (2019). The whole atmosphere community climate model version 6 (WACCM6). *Journal of Geophysical Research: Atmospheres*, *124*(23), 12380–12403.

Gronoff, G., Berkoff, T., Knowland, K. E., Lei, L., Shook, M., Fabbri, B., et al. (2021). Case study of stratospheric Intrusion above Hampton, Virginia: lidar-observation and modeling analysis. *Atmospheric Environment*, *259*, 118498.

Heck, W. W., Taylor, O. C., Adams, R., Bingham, G., Miller, J., Preston, E., & Weinstein, L. (1982). Assessment of Crop Loss from Ozone. *Journal of the Air Pollution Control Association*, *32*(4), 353–361. https://doi.org/10.1080/00022470.1982.10465408

Holton, J. R., Haynes, P. H., McIntyre, M. E., Douglass, A. R., Rood, R. B., & Pfister, L. (1995). Stratosphere-troposphere exchange. *Reviews of Geophysics*, *33*(4), 403. https://doi.org/10.1029/95RG02097

Hsu, J., Prather, M. J., & Wild, O. (2005). Diagnosing the stratosphere-to-troposphere flux of ozone in a chemistry transport model. *Journal of Geophysical Research: Atmospheres*, *110*(D19).

Jaffe, D. A., & Wigder, N. L. (2012). Ozone production from wildfires: A critical review. *Atmospheric Environment*, *51*, 1–10.

Jing, P., Cunnold, D. M., Wang, H. J., & Yang, E. S. (2004). Isentropic cross-tropopause ozone transport in the Northern Hemisphere. *Journal of the Atmospheric Sciences*, *61*(9), 1068–1078.

Johnson, W. B., & Viezee, W. (1981). Stratospheric ozone in the lower troposphere —I. Presentation and interpretation of aircraft measurements. *Atmospheric Environment (1967)*, *15*(7), 1309–1323. https://doi.org/10.1016/0004-6981(81)90325-5

Langford, A. O., Aikin, K. C., Eubank, C. S., & Williams, E. J. (2009). Stratospheric contribution to high surface ozone in Colorado during springtime. *Geophysical Research Letters*, *36*(12).

Langford, A. O., Senff, C. J., Alvarez Ii, R. J., Brioude, J., Cooper, O. R., Holloway, J. S., et al. (2015). An overview of the 2013 Las Vegas Ozone Study (LVOS): Impact of stratospheric intrusions and long-range transport on surface air quality. *Atmospheric Environment*, *109*, 305–322.

Lee, J. (2023). *Data: The Evolutions and Large-scale Mechanisms of Summer Stratospheric Ozone Intrusion across Global Hotspots.* Columbia University Academic Commons. https://doi.org/10.7916/5pcm-er89

Lefohn, A. S., Wernli, H., Shadwick, D., Limbach, S., Oltmans, S. J., & Shapiro, M. (2011). The importance of stratospheric–tropospheric transport in affecting surface ozone concentrations in the western and northern tier of the United States. *Atmospheric Environment*, *45*(28), 4845–4857.

Lefohn, A. S., Wernli, H., Shadwick, D., Oltmans, S. J., & Shapiro, M. (2012). Quantifying the importance of stratospheric-tropospheric transport on surface ozone concentrations at high-and low-elevation monitoring sites in the United States. *Atmospheric Environment*, *62*, 646–656.

Li, D., Bian, J., & Fan, Q. (2015). A deep stratospheric intrusion associated with an intense cut-off low event over East Asia. *Science China Earth Sciences*, *58*, 116–128.

Lin, M., Fiore, A. M., Cooper, O. R., Horowitz, L. W., Langford, A. O., Levy, H., et al. (2012). Springtime high surface ozone events over the western United States: Quantifying the role of stratospheric intrusions. *Journal of Geophysical Research: Atmospheres*, *117*(D21).

Lin, M., Fiore, A. M., Horowitz, L. W., Langford, A. O., Oltmans, S. J., Tarasick, D., & Rieder, H. E. (2015). Climate variability modulates western US ozone air quality in spring via deep stratospheric intrusions. *Nature Communications*, *6*(1), 7105. https://doi.org/10.1038/ncomms8105

Lu, X., Zhang, L., Yue, X., Zhang, J., Jaffe, D. A., Stohl, A., et al. (2016). Wildfire influences on the variability and trend of summer surface ozone in the mountainous western United States. *Atmospheric Chemistry and Physics*, *16*(22), 14687–14702.

Mahlman, J. D. (1997). Dynamics of transport processes in the upper troposphere. *Science*, *276*(5315), 1079–1083.

Mehmood, T., Ahmad, I., Bibi, S., Mustafa, B., & Ali, I. (2020). Insight into monsoon for shaping the air quality of Islamabad, Pakistan: Comparing the magnitude of health risk associated with PM $_{10}$ and PM $_{2.5}$ exposure. *Journal of the Air & Waste Management Association*, *70*(12), 1340–1355. https://doi.org/10.1080/10962247.2020.1813838

Murray, L. T. (2016). Lightning NO x and impacts on air quality. *Current Pollution Reports*, *2*, 115–133.

Ott, L. E., Duncan, B. N., Thompson, A. M., Diskin, G., Fasnacht, Z., Langford, A. O., et al. (2016). Frequency and impact of summertime stratospheric intrusions over Maryland during DISCOVER-AQ (2011): New evidence from NASA's GEOS-5 simulations. *Journal of Geophysical Research: Atmospheres*, *121*(7), 3687–3706.

Pan, L. L., Homeyer, C. R., Honomichl, S., Ridley, B. A., Weisman, M., Barth, M. C., et al. (2014). Thunderstorms enhance tropospheric ozone by wrapping and shedding stratospheric air. *Geophysical Research Letters*, *41*(22), 7785–7790.

Phoenix, D. B., Homeyer, C. R., Barth, M. C., & Trier, S. B. (2020). Mechanisms Responsible for Stratosphere-to-Troposphere Transport Around a Mesoscale Convective System Anvil. *Journal of Geophysical Research: Atmospheres*, *125*(10). https://doi.org/10.1029/2019JD032016

Poulida, O., Dickerson, R. R., & Heymsfield, A. (1996). Stratosphere-troposphere exchange in a midlatitude mesoscale convective complex: 1. Observations. *Journal of Geophysical Research: Atmospheres*, *101*(D3), 6823–6836. https://doi.org/10.1029/95JD03523

Price, J. D., & Vaughan, G. (1993). The potential for stratosphere-troposphere exchange in cut-off-low systems. *Quarterly Journal of the Royal Meteorological Society*, *119*(510), 343–365.

Pye, J. M. (1988). Impact of Ozone on the Growth and Yield of Trees: A Review. *Journal of Environmental Quality*, *17*(3), 347–360. https://doi.org/10.2134/jeq1988.00472425001700030003x

Reich, P. B. (1987). Quantifying plant response to ozone: a unifying theory. *Tree Physiology*, *3*(1), 63–91. https://doi.org/10.1093/treephys/3.1.63

Reichler, T., Dameris, M., & Sausen, R. (2003). Determining the tropopause height from gridded data. *Geophysical Research Letters*, *30*(20).

Rodwell, M. J., & Hoskins, B. J. (2001). Subtropical anticyclones and summer monsoons. *Journal of Climate*, *14*(15), 3192–3211.

Schoeberl, M. R., & Hartmann, D. L. (1991). The Dynamics of the Stratospheric Polar Vortex and Its Relation to Springtime Ozone Depletions. *Science*, *251*(4989), 46–52. https://doi.org/10.1126/science.251.4989.46

Shapiro, M. A. (1980). Turbulent mixing within tropopause folds as a mechanism for the exchange of chemical constituents between the stratosphere and troposphere. *Journal of Atmospheric Sciences*, *37*(5), 994–1004.

Škerlak, B., Sprenger, M., & Wernli, H. (2014). A global climatology of stratosphere–troposphere exchange using the ERA-Interim data set from 1979 to 2011. *Atmospheric Chemistry and Physics*, *14*(2), 913–937. https://doi.org/10.5194/acp-14-913-2014

Škerlak, B., Sprenger, M., Pfahl, S., Tyrlis, E., & Wernli, H. (2015). Tropopause folds in ERA-Interim: Global climatology and relation to extreme weather events. *Journal of Geophysical Research: Atmospheres*, *120*(10), 4860–4877.

Škerlak, B., Pfahl, S., Sprenger, M., & Wernli, H. (2019). A numerical process study on the rapid transport of stratospheric air down to the surface over western North America and the Tibetan Plateau. *Atmospheric Chemistry and Physics*, *19*(9), 6535–6549. https://doi.org/10.5194/acp-19-6535-2019

Smith, G., Coulston, J., Jepsen, E., & Prichard, T. (2003). A national ozone biomonitoring program–results from field surveys of ozone sensitive plants in northeastern forests (1994–2000). *Environmental Monitoring and Assessment*, *87*, 271-291.

Smith, W. P., Pan, L. L., Honomichl, S. B., Chelpon, S. M., Ueyama, R., & Pfister, L. (2021). Diagnostics of Convective Transport Over the Tropical Western Pacific From Trajectory Analyses. *Journal of Geophysical Research: Atmospheres*, *126*(17). https://doi.org/10.1029/2020JD034341

Solberg, S., Hov, Ø., Søvde, A., Isaksen, I. S. A., Coddeville, P., De Backer, H., et al. (2008). European surface ozone in the extreme summer 2003. *Journal of Geophysical Research: Atmospheres*, *113*(D7).

Sprenger, M., & Wernli, H. (2003). A northern hemispheric climatology of cross-tropopause exchange for the ERA15 time period (1979–1993). *Journal of Geophysical Research: Atmospheres*, *108*(D12).

Sprenger, M., Croci Maspoli, M., & Wernli, H. (2003). Tropopause folds and cross-tropopause exchange: A global investigation based upon ECMWF analyses for the time period March 2000 to February 2001. *Journal of Geophysical Research: Atmospheres*, *108*(D12).

Stohl, A., Spichtinger-Rakowsky, N., Bonasoni, P., Feldmann, H., Memmesheimer, M., Scheel, H. E., et al. (2000). The influence of stratospheric intrusions on alpine ozone concentrations. *Atmospheric Environment*, *34*(9), 1323–1354.

Stohl, A., Wernli, H., James, P., Bourqui, M., Forster, C., Liniger, M. A., et al. (2003). A New Perspective of Stratosphere–Troposphere Exchange. *Bulletin of the American Meteorological Society*, *84*(11), 1565–1574. https://doi.org/10.1175/BAMS-84-11-1565

Tang, Q., Prather, M. J., & Hsu, J. (2011). Stratosphere-troposphere exchange ozone flux related to deep convection. *Geophysical Research Letters*, *38*(3).

Tilmes, S., Lamarque, J.-F., Emmons, L. K., Kinnison, D. E., Marsh, D., Garcia, R. R., et al. (2016). Representation of the community earth system model (CESM1) CAM4-chem within the chemistry-climate model initiative (CCMI). *Geoscientific Model Development*, *9*(5), 1853–1890.

Trickl, T., Vogelmann, H., Giehl, H., Scheel, H.-E., Sprenger, M., & Stohl, A. (2014). How stratospheric are deep stratospheric intrusions? *Atmospheric Chemistry and Physics*, *14*(18), 9941–9961.

Tyrlis, E., & Lelieveld, J. (2013). Climatology and dynamics of the summer Etesian winds over the eastern Mediterranean. *Journal of the Atmospheric Sciences*, *70*(11), 3374–3396.

Wakamatsu, S., Uno, I., Ueda, H., Uehara, K., & Tateishi, H. (1989). Observational study of stratospheric ozone intrusions into the lower troposphere. *Atmospheric Environment (1967)*, *23*(8), 1815–1826.

Wang, X., Wu, Y., Randel, W., & Tilmes, S. (2020). Stratospheric contribution to the summertime high surface ozone events over the western united states. *Environmental Research Letters*, *15*(10), 1040a6. https://doi.org/10.1088/1748-9326/abba53

WHO (2021). WHO global air quality guidelines: particulate matter (PM2. 5 and PM10), ozone, nitrogen dioxide, sulfur dioxide and carbon monoxide: executive summary.

WMO (1957). Meteorology—A three-dimensional science: Second session of the commission for aerology. *WMO Bull.*, *4*(4), 134–138.

Wu, Y., Chen, G., Taylor, L., & Zhang, P. (2018). On the linkage between the Asian summer monsoon and tropopause folds. *Journal of Geophysical Research: Atmospheres*, *123*(4), 2037–2049.

Xiong, X., Liu, X., Wu, W., Knowland, K. E., Yang, Q., Welsh, J., & Zhou, D. K. (2022). Satellite observation of stratospheric intrusions and ozone transport using CrIS on SNPP. *Atmospheric Environment*, *273*, 118956.

Yang, H., Chen, G., Tang, Q., & Hess, P. (2016). Quantifying isentropic stratosphere-troposphere exchange of ozone. *Journal of Geophysical Research: Atmospheres*, *121*(7), 3372–3387.

Zanis, P., Trickl, T., Stohl, A., Wernli, H., Cooper, O., Zerefos, C., et al. (2003). Forecast, observation and modelling of a deep stratospheric intrusion event over Europe. *Atmospheric Chemistry and Physics*, *3*(3), 763–777.

Zanis, P., Hadjinicolaou, P., Pozzer, A., Tyrlis, E., Dafka, S., Mihalopoulos, N., & Lelieveld, J. (2014). Summertime free-tropospheric ozone pool over the eastern Mediterranean/Middle East. *Atmospheric Chemistry and Physics*, *14*(1), 115–132.

Zhao, K., Huang, J., Wu, Y., Yuan, Z., Wang, Y., Li, Y., et al. (2021). Impact of stratospheric intrusions on ozone enhancement in the lower troposphere and implication to air quality in Hong Kong and other South China regions. *Journal of Geophysical Research: Atmospheres*, *126*(18), e2020JD033955.

AGU PUBLICATIONS

*JGR Atmosphere*

Supporting Information for

**The Evolutions and Large-scale Mechanisms of Summer Stratospheric Ozone Intrusion across Global Hotspots**

J. Lee[1], Y. Wu[1], and X. Wang[2]

[1]Lamont-Doherty Earth Observatory of Columbia University, New York, NY

[2]National Center for Atmospheric Research, Boulder, CO

## Contents of this file

Figures S1 to S3

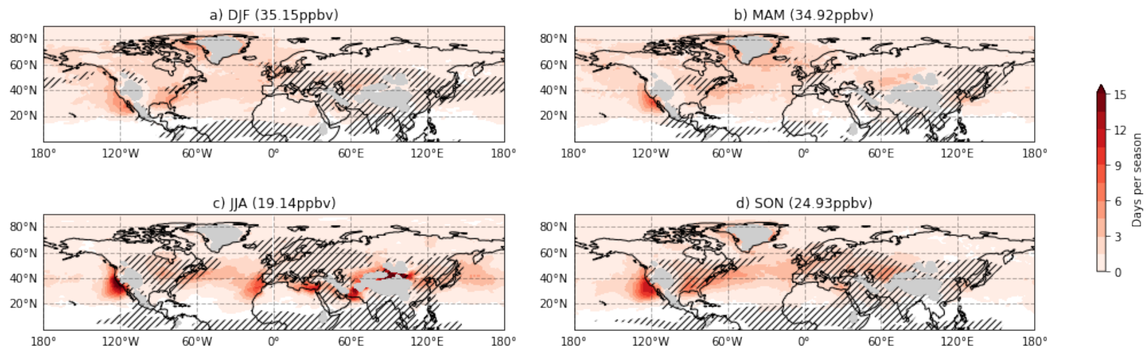


**Figure S1.** The average days per season when 850 hPa $O_3S$ exceeds 99% of NH $O_3S$ each season. The 99% $O_3S$ threshold across the entire NH for each season is written in parentheses. Red shadings are days per season, and gray shadings are masked topography. Regions where R-squared values between anomalous $O_3$ and $O_3S$ below 0.5 are hatched.

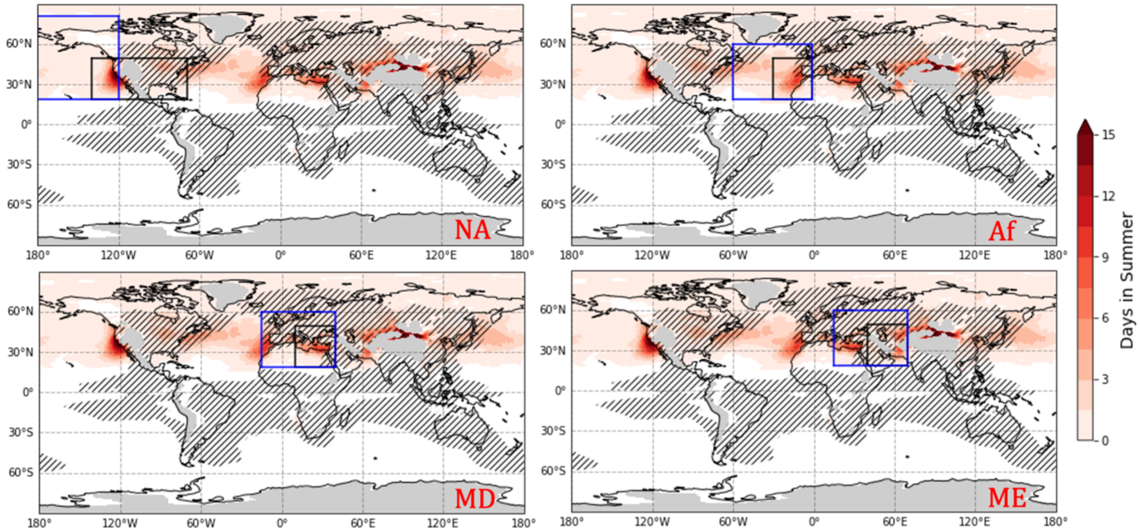


**Figure S2.** Boxes are drawn on top of Fig. 1 for MCA and composite analysis. Black boxes show where MCA is conducted for each hotspot. They all have the same latitude range of 20º-50ºN. The ranges of longitude for each hotspot are NA (140º-70ºW), Af (30ºW-0º), MD (10º-40ºE), and ME (40º-70ºE). Blue boxes show where stratospheric ozone intrusion speed has been estimated from box-averaged $O_3S$ anomaly. The latitude range for NA is 20º-80ºN, while others all have the same latitude range of 20º-60ºN. The ranges of longitude for each hotspot are NA (180º-120ºW), Af (60ºW-0º), MD (15ºW-40ºE), and ME (15º-70ºE).

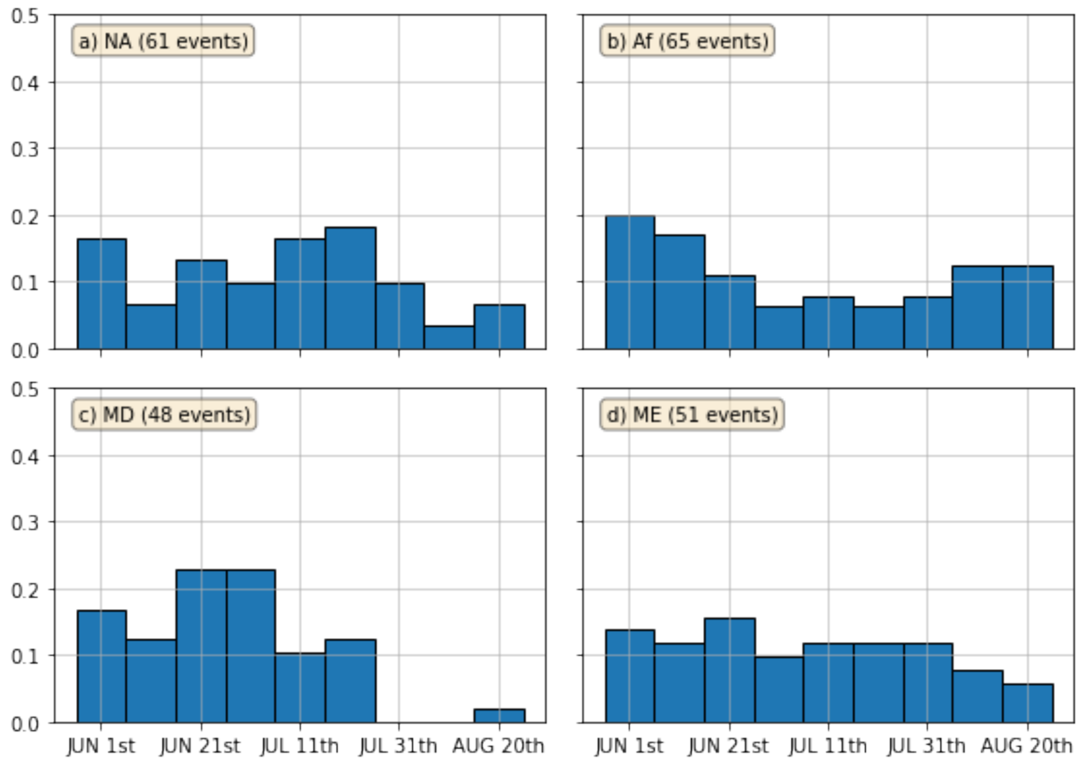


**Figure S3.** The density histogram of the start date of extreme events for every global hotspot. The extreme events are defined following section 3.2 and calculated for the MCA's leading mode. Each bin is 10 days long except for the last bin, which is 12 days. Each hotspot's total number of events is written in the parenthesis next to the hotspot name.